

Delocalization Effect Promoted the Indoor Air Purification via Directly Unlocking the Ring-Opening Pathway of Toluene

Wenqiang Qu,[†] Penglu Wang,[†] Min Gao, Jun-ya Hasegawa, Zhi Shen, Qing Wang, Ruomei Li, and Dengsong Zhang*



Cite This: *Environ. Sci. Technol.* 2020, 54, 9693–9701



Read Online

ACCESS |

Metrics & More

Article Recommendations

Supporting Information

ABSTRACT: The ring-opening process was generally considered as the rate-determining step for aromatic volatile organic compound photocatalytic degradation. A sophisticated and intensive degradation pathway is critical to the poor removal efficiency and low mineralization. In the present contribution, we successfully tailored and identified the ring-opening pathway of toluene elimination by electron delocalization in a borocarbonitride photocatalyst. By means of modulation of the dopant coordination configuration and electron geometry in the catalyst, the lone electrons of carbon transform into delocalized counterparts, sequentially elevating the interaction between the toluene molecules and photocatalyst. The aromatic ring of toluene can be attacked directly in the effect of electron delocalization without engendering additional intermediate species, significantly facilitating the removal and mineralization of toluene. This unprecedented route-control strategy alters the aromatic-ring-based reaction behavior from toluene to CO₂ and paves a way to purify the refractory pollutants from the top design.



INTRODUCTION

The ever-growing demand of the indoor environment to modern society has never been so urgent for clean air.^{1,2} Toluene, a ubiquitous volatile organic compound (VOC), has aroused extensive attention for its conspicuous detriment to the environment and health, even in an infinitesimal concentration.^{3,4} Conventionally, an industrial technique of catalytic combustion has been applied for toluene with a high concentration from industrial emission,^{5–7} which is not suitable for indoor air purification under ambient conditions. In this respect, photocatalysis technology has been deemed as an efficient strategy for the removal of dilute toluene in a resource-conserving and environmentally friendly manner.^{8–10}

Considerable effort has been paid to investigate the reaction pathway of toluene degradation, which has still been a persistent challenge for the underlying mechanism.^{11–15} Notably, it is universally acknowledged that the ring-opening process is regarded as the rate-limiting step toward toluene removal in photocatalysis.^{12,16,17} Simultaneously, massive and diverse uphill reactions are corroborated in the ring-opening process, while the competitive adsorption between the numerously generated intermediate species engenders the desorption of the derivatives with weak adsorption capability, subsequently encountering a low mineralization.^{18–20} Therefore, exploring and tailoring a more efficient ring-opening pathway will be one of prominent significance for the photocatalytic elimination of toluene.

As a result of its advantages, such as abundance and strong oxidative ability, TiO₂ has been intensively investigated in the field of indoor environment remediation.^{21,22} However, limitation of ultraviolet (UV) response constitutes a significant hurdle to directly use the indoor environment light without an extra irradiation source.^{23–25} Additionally, one long-lasting unsolved roadblock lying in the further application of TiO₂ is the rapid deactivation for elimination of VOCs, which is attributed to the accumulation of carbonaceous intermediates and coke.^{18,26,27} Because the strong interaction between the intermediates and photocatalyst and the scarcity of reactive oxygen species hinder the removal of carbonaceous intermediates in time, the active sites of the photocatalyst are blocked with the growth of the intermediates, thus encountering the performance handicaps.^{28–30} As a result, it plays a pivotal practical role in developing a photocatalyst with high durability and visible-light response for indoor air purification.

Boron nitride (BN) has been confirmed to be a two-dimensional metal-free catalyst with superior resistance of

Received: May 7, 2020

Revised: June 2, 2020

Accepted: June 29, 2020

Published: June 29, 2020



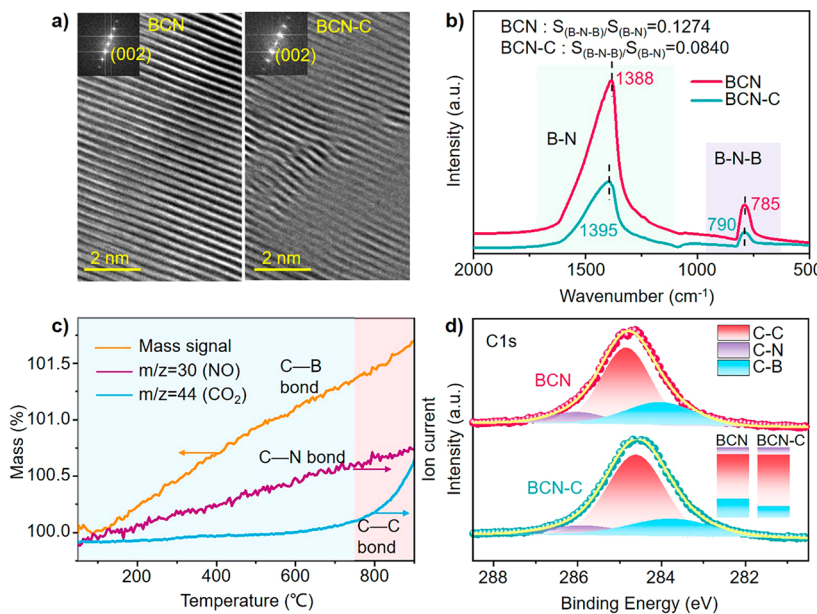


Figure 1. (a) HRTEM image and (b) FTIR spectra of BCN and BCN-C. (c) *In situ* observation of BCN thermal treatment by TG-MS versus calcination temperatures under an air atmosphere with a heating rate of 5 °C/min. (d) High-resolution XPS spectra of C 1s toward BCN-C and BCN.

carbonaceous intermediates and coke deposition in our previous works.^{31–33} Intriguingly, this insulator material transforms into a borocarbonitride (BCN) photocatalyst with visible-light response after carbon doping and has aroused tremendous attention in the field of photocatalytic reduction, such as CO₂ fixation and water-splitting reaction.^{34,35} Hence, BCN has potential in pollutant control via photocatalysis. However, the atomic structure of BCN is still ambiguous, and the energy band structure makes it unfavorable for photocatalytic oxidation, where the valence band would always shift upward with the carbon doping in BCN.^{36–39}

In this study, we successfully tailored and identified the ring-opening pathway of toluene removal by controlling the shape of the dopant coordination structure in BCN, where the carbon chains transformed into π -conjugate carbon ring configurations and the lone electrons of carbon turned into delocalized electrons in BCN. Experimental results revealed that the delocalized electrons were favorable for facilitating photogenerated charge separation and the formation of reactive oxygen species. Furthermore, the enhanced interaction between toluene molecules and photocatalyst and the direct ring-opening pathway of toluene were confirmed, significantly improving the toluene degradation behavior.

EXPERIMENTAL SECTION

Chemicals and Materials. Boric acid, urea, glucose, and hydrochloric acid (37%) were purchased from Sinopharm Chemical Reagent Co., Ltd. (China). All of the chemical reagents were analytical-grade and used as received without further purification.

Synthesis of BCN. The BCN samples were typically prepared by a pyrolysis method.⁴⁰ An amount of glucose was mixed with 3.551 g of boric acid and 4 g of urea. After fully ground, the precursor was transferred to a corundum boat with a cover and then put into a tube furnace. Argon was first introduced to completely expel oxygen in the tube before heating. Subsequently, the precursor was maintained at 1250

°C for 300 min at a heating rate of 4 °C min⁻¹. The obtained solid was ground and washed with 0.2 M HCl solution to remove the impurities, followed by washing with deionized water several times. Finally, the samples were dried at 80 °C for 8 h, and the as-prepared samples were labeled as BCN- x , where x was the glucose weight in percent of boron oxide (3.551 g of boric acid was equivalent to 2 g of boron oxide). In this work, BCN-10 (denoted as BCN) was selected as the representative sample as a result of its best oxidation capability among BCN- x , and BCN-30 was selected as a higher reference sample, denoted as BCN-H.

Synthesis of BCN-C. For preparation of BCN-C, a post-process was performed to the BCN sample. A total of 0.5 g of BCN powder was calcined under static air at 750 °C for 3 h. The obtained powder was denoted as BCN-C-B and was washed by 0.2 M HCl solution, deionized water, and ethanol, separately. The final obtained sample was labeled as BCN-C.

Photocatalytic Gas Toluene Removal. A total of 80 mg of sample catalyst was evenly dispersed on a 64 mm diameter quartz plate with water as the medium, dried in a 60 °C oven, and placed in a 275 mL steel closed reactor, where a magneton was placed to stir and accelerate the gas flow. After high-purity air aeration of 20 min, 0.1 μ L of liquid toluene was pumped into the reactor and absorbed for 30 min. A 300 W xenon lamp (PLS-SXE300, Perfect Light, Beijing, China) equipped with a 420 nm cutoff filter was used as the light source. The intensity of the light flux was measured to be 150 mW/cm² by an optical power meter (PL-MW2000, Perfect Light). A gas chromatograph (GC 9890B equipped with a flame ionization detector and methane-reforming furnace) was applied to measure the concentrations of toluene and carbon dioxide.

Thermogravimetry–Mass Spectrometry (TG–MS) Measurement. The pyrolysis experiment was conducted using a TG–MS analyzer (STA 449 F1 Jupiter, NETZSCH, TG/DTA; OmniStar, MS) in an air atmosphere with a heating rate of 5 °C min⁻¹ from room temperature to 900 °C.

Gas Chromatography–Mass Spectrometry (GC–MS) Measurement. Under the same conditions with photo-

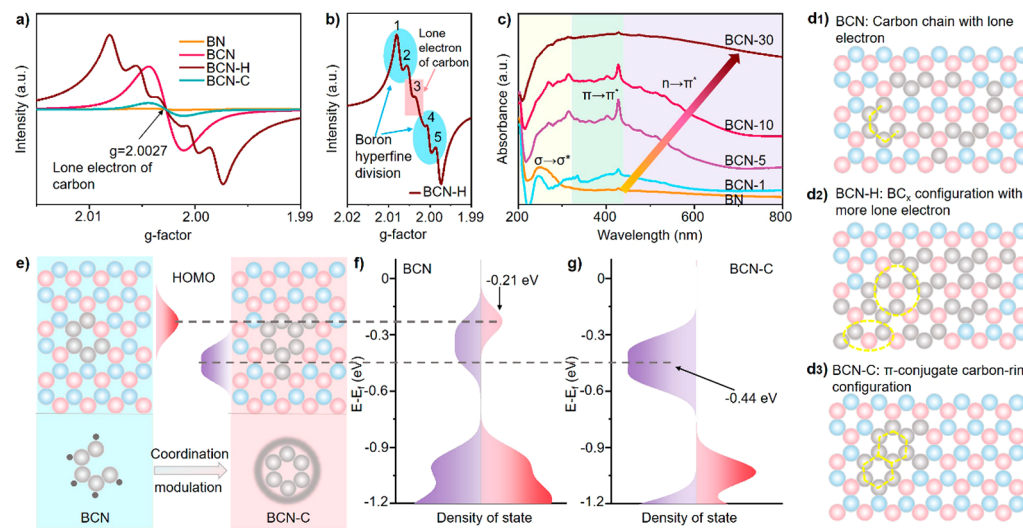


Figure 2. (a) EPR spectra of BN, BCN, BCN-H, and BCN-C under 100 K. (b) Detailed EPR spectra of BCN-H under 100 K. (c) DRS spectra of BCN with different carbon contents using BaSO₄ as a reference. BCN with different carbon contents was labeled as BCN-x, where x is the weight ratio of raw materials between glucose and boron oxide. (d) Atomic structure of (d1) BCN with carbon chain configuration, (d2) BCN-H with BC_x configuration, and (d3) BCN-C with π -conjugated carbon ring configuration. The boron (red), nitrogen (blue), and carbon (black) atoms were exhibited. (e) Simplified models of BCN and BCN-C. Calculated PDOS of (f) BCN and (g) BCN-C.

catalytic gas toluene removal evaluation, 250 μ L of reaction outlet gas was injected to GC-MS (Agilent Technologies 7890B, Santa Clara, CA, U.S.A.) equipped with an automated thermal desorber (UNITY-xr, Markes International, U.K.) every 30 min.

Toluene Temperature-Programmed Desorption-Mass Spectrometry (Toluene-TPD-MS). The toluene-TPD was performed on a Tianjin XQTP-5080 auto-adsorption apparatus with an OMNI Star magic angle spinning (MAS) spectrum. A total of 80 mg of catalyst was weighed and placed in a quartz tube. After 10 min of argon (30 mL/min) purging, the catalyst was heated to 300 °C for 30 min and then restored to room temperature. Toluene/N₂ standard gas (1000 ppm, 50 mL/min) was injected for 1 h to balance the adsorption and desorption of the catalyst, and then the inlet gas was converted to helium. The temperature was programmed to rise to 300 °C at a rate of 10 °C/min, while the thermal conductivity detector (TCD) signal and the desorption gas information in the MAS were recorded.

In Situ Diffuse Reflectance Infrared Fourier Transform Spectroscopy (DRIFTS). After 20 min of helium purging to remove the gas from the reactor chamber, the sample was heated to 200 °C and pretreated for 20 min. When the temperature was cooled to the 30 °C, the baseline was collected and the reaction gas of toluene was transferred to the reaction chamber, which was adsorbed for 20 min. Then, helium was purged for 20 min to remove impurities and weakly adsorbed substances in the reactor chamber. At this point, the catalyst surface after adsorption of toluene was used to collect the background, and visible light was introduced to collect the infrared information on the catalyst surface every 4 min.

RESULTS AND DISCUSSION

Electronic Structure Characterization. As uncovered by X-ray diffraction (XRD) patterns (Figure S1 of the Supporting Information), the diffraction peaks of both BCN and BCN-C coincided well with those of h-BN [powder diffraction file (PDF) 34-0421]. The main diffraction peak located at 26.6° assigned to the (002) plane was weakened in BCN-C, in which

the intensity ratio of (002)/(100) plane was decreased from BCN (12.35) to BCN-C (11.54). A transmission electron microscopy (TEM) image (Figure S2 of the Supporting Information) exhibited the morphology of extensively stacked crystalline nanosheets of BCN-C, and energy-dispersive X-ray spectroscopy (EDS) mapping (Figure S3 of the Supporting Information) revealed the carbon element evenly distributed in BCN-C. High-resolution transmission electron microscopy (HRTEM) images (Figure 1a) and the fast Fourier transform (FFT) patterns displayed the (002) plane of BCN and BCN-C. Surprisingly, in comparison to BCN (Figure S4 of the Supporting Information), the lattice of BCN-C suffered a severe distortion (Figure S5 of the Supporting Information), which might result from the formation of a modulated structure and the subsequently weaken XRD intensity of the (002) plane.

Fourier transform infrared (FTIR) spectra (Figure 1b) displayed two prototypical characteristic peaks that can be ascribed to B-N and B-N-B bonds. The vibrations of C-N or C-B bonds cannot be appreciable for being overlapped by B-N bands.⁴¹ Moreover, the positions of B-N (1388 cm⁻¹) and B-N-B (785 cm⁻¹) in BCN showed a blue shift to 1395 and 790 cm⁻¹ in BCN-C, respectively, suggesting that BCN-C was more thermodynamically stable. Furthermore, it was found that the peak area ratio of B-N-B/B-N among BCN-C (0.084) was much lower than that in BCN (0.1274), suggesting the existence of a process with chemical bond breaking and recombination during the post-treatment.

To verify the exact behavior of chemical bonds, the post-process was *in situ*-observed by TG-MS (Figure 1c) under the same thermal treatment conditions. The mass variation and possible substances generated were distinguished among two regions, including low temperature (50–750 °C) and high temperature (750–900 °C). The different oxidized behaviors among B, N, and C come from the distinct bond energy, where B-N > C-C > C-B ≈ C-N.^{37,42} Few CO₂ was stably generated at the low-temperature zone corresponding to the decomposition of C-N and C-B bonds, while the CO₂ production drastically increased at the high-temperature

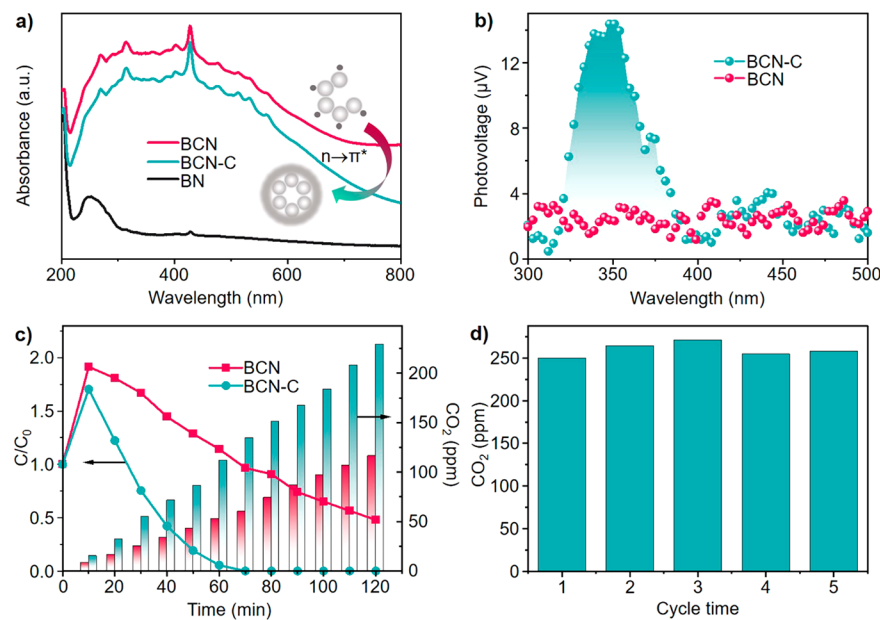


Figure 3. (a) UV-vis diffuse reflectance spectra of BCN-C, BCN, and BN using BaSO₄ as a reference. (b) Surface photovoltage spectra of BCN-C and BCN. (c) Photocatalytic degradation performance of BCN-C and BCN toward gas toluene under irradiation with a 300 W xenon lamp with a 420 nm cutoff filter. (d) Repeated cycles of photocatalytic degradation of gaseous toluene on BCN-C.

zone, owing to the break of the C–C bond. The continuously increasing mass of BCN and generated NO can be respectively ascribed to the oxidation of B (B₂O₃ was further confirmed by XRD in Figure S6 of the Supporting Information) and the N element. The constant production rate of B₂O₃ indicated that the same fracture behavior of the chemical bond maintained on the B element in the whole temperature region as well as the NO generation behavior happened on the N element, suggesting that only C–B and C–N were taken apart, while the B–N bond was stable enough to remain in BCN crystals. The other gases possibly generated under the treatment condition were monitored simultaneously (Figure S7 of the Supporting Information), which could be ignored as their trace content. X-ray photoelectron spectroscopy (XPS; Figure 1d and Figure S8 of the Supporting Information) spectra further confirmed the increasing proportion of C–C, B–N, and the carbon content (Tables S1–S4 of the Supporting Information) in BCN-C, which was consistent with the TG–MS result that C–B and C–N bonds were depleted in the treatment.

The electronic geometry was then investigated by low-temperature electron paramagnetic resonance (EPR) spectra (Figure 2a and Figure S9 of the Supporting Information) at 100 K. The electronic geometry of BCN was first identified, and one single Lorentzian line with a *g* value of 2.0027 was observed in BCN compared to the BN sample, which can be assigned to the unpaired electron of carbon when the heteroelement incorporation was in a commonly sp²-hybridized state.⁴⁰ The distinctly increasing EPR signal revealed that more lone electrons resided in the BCN structure with the increasing carbon-doping content. Interestingly, the EPR spectra of BCN-H (a much higher carbon content of the BCN sample; Figure 2b) turned into five splitting lines and still kept a *g* value of 2.0027, which was derived from the superposition with the hyperfine splitting of ¹¹B (four of the five lines) and the lone-electron signal of carbon (one of the five lines).^{43,44} This result indicated that a BC_x configuration was constituted and the localized lone electron of carbon that

interacted with ¹¹B was critical to this hyperfine splitting. Therefore, the carbon incorporation preferred to substitute the N site with massive localized lone electrons. Ultraviolet-visible (UV-vis) diffuse reflectance spectroscopy (DRS; Figure 2c) was employed to further confirm the local electron state in BCN with different carbon contents. The entire DRS of BCN was derived from σ → σ* in B–N (around 200–300 nm), π → π* (around 300–430 nm), and n → π* in the lone electron of carbon (above 430 nm).^{45,46} The weakened peak intensity of σ → σ* in the B–N bond compared to BN implied that the incorporation of carbon cleaved the B–N bond and, thus, formed C–B or C–N bonds. Moreover, the entire DRS spectra of BCN expressed an obvious red shift with the increasing carbon content that mainly derived from n → π* (above 430 nm) in the unpaired electron of carbon. Above all, the carbon coordination configurations of BCN (Figure 2d1) and BCN-H (Figure 2d2) were authenticated, and the process of carbon incorporation into the BN crystal was exhibited in Figure S10 of the Supporting Information, where carbon was susceptible to substitute the N atom and form carbon chains (C ≥ 1) with substantial localized lone electrons in BCN.

For the coordination configuration and electronic geometry in BCN-C, in combination with the preceding observations that the breaking of C–B and C–N bonds led to an increasing proportion of the C–C bond and a slight rise of the carbon content after the post-process, the lone electron EPR signal attenuated significantly and no signal of boron was found in BCN-C, indicating that the localized lone electrons transformed into a delocalized electron and the in-plane π-conjugated ring configuration was formed (Figure 2d3). More importantly, it transpired that this unique structure cannot be realized by direct heteroelement doping.

Above all, the coordination structure of BCN and BCN-C could be summarized that carbon was prone to substitute a N atom in a carbon-chain state in BCN, while C preferred to form in-plane π-conjugated rings with an aggregated state in BCN-C. Moreover, the accumulated lone electrons trans-

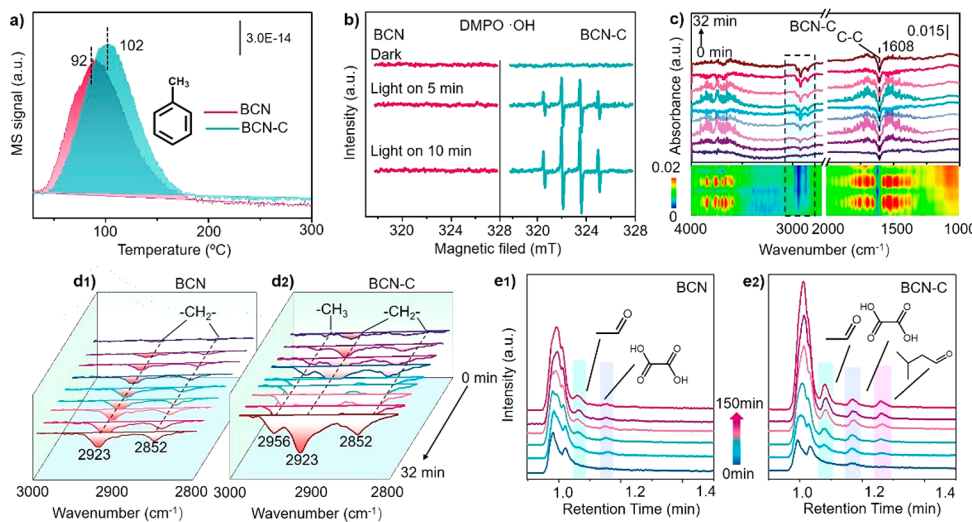


Figure 4. (a) MS signal of toluene-TPD-MS profiles over BCN and BCN-C. (b) EPR spectra of DMPO- \cdot OH under visible irradiation of BCN-C and BCN. (c) *In situ* DRIFTS spectra of toluene degradation over BCN-C and the corresponding mapping image of the reaction process. The sample was pretreated at 200 °C under helium purging for 20 min and subsequently adsorbed with 50 ppm of gas toluene at 25 °C for 20 min before illumination. (d) *In situ* DRIFTS spectra of toluene degradation between 2800 and 3000 cm⁻¹ over (d1) BCN and (d2) BCN-C. (e) GC-MS profiles with a prolonged reaction time upon (e1) BCN and (e2) BCN-C.

formed into delocalized electrons. Density functional theory (DFT) calculations were carried out to explore the electronic properties according to the simplified models of BCN and BCN-C catalysts (panels e–g of Figure 2). According to the spin-polarized partial density of states (PDOS) corresponding to C (red curve) and B and N (purple curve) atoms for the catalysts, an unoccupied spin-down defect level of C appeared upon the valence band of h-BN and below the Fermi level (0 eV), which engendered the position of the highest occupied molecular orbital (HOMO) shifting upward and a valence band located at -0.21 eV. Nevertheless, this defect level was absent after the formation of the in-plane π -conjugated structure in BCN-C, and BCN-C kept an inherent lower valence band position at -0.44 eV. In this case, the HOMO orbital of BCN was determined by carbon, triggering a higher valence band position and attenuating oxidation potential. Nevertheless, the HOMO state of BCN-C hinged on BN, being immune to the influence of carbon, subsequently maintaining a lower valence state and affording an enhanced oxidation state for photocatalysts.

Photocatalytic Toluene Removal. The UV-vis diffuse reflectance spectrum (Figure 3a) was employed again to distinguish the light harvest capacity. BCN-C performed a weakened light harvest ability, although with a higher carbon content (Figure S11 of the Supporting Information). The attenuation of the light absorption threshold was attributed to the reduced lone electron, which was sequentially responsible for the decrease of $n \rightarrow \pi^*$. The surface photovoltage (Figure 3b) spectra and transient photocurrent (Figure S12 of the Supporting Information) indicated the migration and spatial redistribution of photogenerated carriers.⁴⁸ BCN-C showed a higher surface photovoltage (SPV) response intensity, while BCN exhibited an almost disappeared SPV signal as a result of the excessive lone electrons in BCN leading to rapid carrier recombination. The transient photocurrent operated under visible light indicated that BCN-C exhibited a much higher photocurrent response, simultaneously. Valence-band XPS (Figure S13 of the Supporting Information) indicated that a higher oxidation capacity was observed over the valence band

of BCN-C (2.40 eV) than BCN (2.17 eV). In combination with the Mott-Schottky plot (Figure S14 of the Supporting Information), the energy band position moved toward a positive direction. Therefore, the delocalized electron in BCN-C has a significant influence on the photoelectric properties of carrier diffusion and energy band.

Under visible light irradiation, BCN-C achieved a remarkable toluene degradation performance with a reaction kinetic constant of 0.040 76 (Figure 3e and Figure S15 of the Supporting Information), which showed a 5-fold enhancement in comparison to BCN. More importantly, the generation of CO₂ was nearly twice for BCN-C than that for BCN, exhibiting a much higher mineralization. The rising concentration of toluene in the first 10 min resulted from tremendous toluene absorbed on the catalyst surface desorbed into the gas phase after illumination. BCN with different carbon contents was also performed to rule out the influence of carbon contents between BCN and BCN-C (Figure S16 of the Supporting Information), where a slow degradation kinetics and low mineralization were revealed on BCN with various carbon contents. Simultaneously, BCN-C showed a remarkable visible light photocatalytic degradation performance toward toluene compared to the popular visible light responsive photocatalysts C₃N₄ and Bi₂WO₆ and other photocatalysts (Figure S17 and Table S5 of the Supporting Information). As a summary of the analytics, the electron delocalization endowed a unique and prominent photocatalytic degradation performance. Furthermore, the durability of BCN-C was confirmed, and a superior performance of mineralization (Figure 3d) was still maintained after 5 cycles of photocatalytic degradation.

In-Depth Mechanism of Photocatalytic Toluene Degradation. To understand the underlying reason for the special performance and durability. The physical/chemical adsorption behavior was first investigated. Brunauer–Emmett–Teller (BET) surface area analysis (Figure S18 of the Supporting Information) showed a smaller physical surface on BCN-C, and the HRTEM image (Figure S19 of the Supporting Information) confirmed the easier stacking between the layers in BCN-C, which might result from the

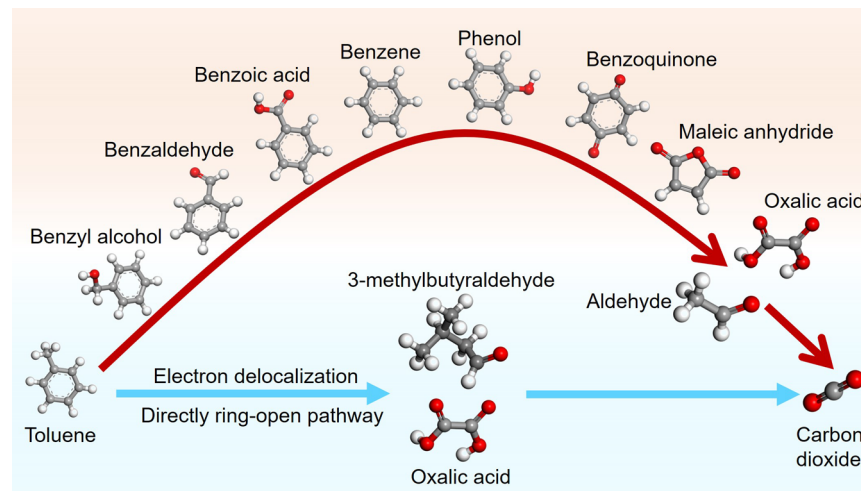


Figure 5. Schematic illustration for different pathways of photocatalytic gas toluene degradation.

interaction of the delocalized electrons between the interlayer. Despite the fact that BCN-C possessed a less physical adsorption surface, toluene-TPD-MS (Figure 4a and Figure S20 of the Supporting Information) indicated more toluene adsorbed on BCN-C. In addition, the toluene desorption temperature over BCN-C ($102\text{ }^{\circ}\text{C}$) was higher than that over BCN ($92\text{ }^{\circ}\text{C}$), revealing a stronger interaction between toluene molecules and BCN-C on the effect of delocalized electrons. Oxygen-TPD (Figure S21 of the Supporting Information) was also carried out to evaluate the chemical adsorption toward O_2 . BCN-C and BCN exhibited a similar adsorption capacity toward O_2 . Reactive oxygen species (ROS) were supposed to be indispensable for photocatalytic degradation. In this regard, *in situ* EPR (Figure 4b and Figure S22 of the Supporting Information) was employed to detect hydroxyl radicals ($\cdot\text{OH}$) and superoxide radicals ($\cdot\text{O}_2^-$). $\cdot\text{O}_2^-$ can be generated in both BCN and BCN-C rapidly with illumination, while $\cdot\text{OH}$ can only be accumulated in BCN-C. Therefore, the electron delocalization strengthened the adsorption behavior toward toluene and boosted the generation of $\cdot\text{OH}$ with little impact on the adsorption and activation of O_2 .

In situ DRIFTS was further performed to realize real-time monitoring of toluene molecules degraded over the surface of BCN and BCN-C. During the adsorption process of toluene, the main accumulated species adsorbed on the catalyst were attributed to hydroxyl, benzyl alcohol, and aromatic ring (Figure S23 and Table S6 of the Supporting Information).^{16,49} After visible light irradiation, the C–C bond of the benzene ring located at 1608 cm^{-1} was rapidly consumed on BCN-C, while the benzene ring on BCN had no obvious consumption (Figure 4c and Figure S24 of the Supporting Information),⁵⁰ suggesting a much higher ring-opening rate of BCN-C. In combination with the mapping image of the reaction process, the intermediate species between 1200 and 2000 cm^{-1} were consumed and supplemented repeatedly, indicating the process of toluene consumption into intermediate species and the digestion of intermediate species, respectively.

It was worth noting that an additional consumption peak at 2956 cm^{-1} assigned to methyl ($-\text{CH}_3$) was only found on BCN-C during the photocatalytic degradation, while two consumption peaks at 2852 and 2923 cm^{-1} attributed to methylene ($-\text{CH}_2-$) were detected on both BCN and BCN-C (panels d1 and d2 of Figure 4).^{51,52} To comprehend this

confusing phenomenon, the peaks among 1200 – 2000 cm^{-1} were distinguished in detail to find the toluene degradation pathway (Figure S25 of the Supporting Information). However, the intermediates on the surface of BCN-C were nearly identical to those on BCN, and the intermediate products were mainly attributed to benzaldehyde, benzoic acid, phenol, benzoquinone, maleic anhydride, and oxalic acid. Furthermore, the intermediates in the gas phase were monitored by gas chromatography–mass spectrometry (GC–MS; panels e1 and e2 of Figure 4 and Figures S26 and S27 of the Supporting Information). It could be mentioned that, apart from carbon dioxide, benzene, oxalic acid, and acetaldehyde, 3-methylbutyraldehyde was also found with the catalysis of BCN-C, which contributed to the fragment produced by direct ring opening of toluene for intact and unoxidized $-\text{CH}_3$. When all of the intermediates were taken into account, a typically similar toluene degradation pathway (Figure 5) took place on both BCN and BCN-C from the oxidation of toluene into benzyl alcohol. Moreover, the differential intermediates among BCN and BCN-C simultaneously confirmed a new ring-opening pathway in which the aromatic ring could directly open over BCN-C.

In combination with the results above, the strong oxidation ability of $\cdot\text{OH}$, generated over BCN-C and enhanced the interaction between the reactants and the catalyst, made it possess the ability to attack the aromatic ring of toluene directly, which was responsible for the rapid consumption of methyl ($-\text{CH}_3$) at 2956 cm^{-1} and the aromatic ring located at 1608 cm^{-1} . The delocalization effect brought out a more efficient and concise ring-opening pathway, producing less carbonaceous intermediates, which was critical to the remarkable durability, high mineralization rate, and immensely enhanced photocatalytic degradation performance. Furthermore, benzene, which was also regarded as the main air pollutant indoors, was selected to verify the conclusion. Without any substituent group, the degradation of benzene can be considered as the aromatic ring-opening process, and the ring-opening capability can be obtained by the conversion of benzene. As expected, the trend of photocatalytic benzene removal was consistent with the tendency in toluene degradation (Figure S28 of the Supporting Information).

Environmental Implications. For photocatalytic purification of gas toluene, one of the most ubiquitous indoor air

pollutants, the rate-limiting step is attributed to the ring-opening process. However, the sophisticated ring-opening pathway engendered a lot of trouble, such as unsatisfied performance, low mineralization, and deactivation of the photocatalyst. In this study, we modulated the electron geometry into delocalized electrons and successfully designed a direct ring-opening pathway for gas toluene removal, significantly improving the air purification performance. This work could provide a fresh idea from the design of the ring-opening pathway to gas toluene elimination as well as deepening the mechanistic comprehension of VOC removal.

■ ASSOCIATED CONTENT

SI Supporting Information

The Supporting Information is available free of charge at <https://pubs.acs.org/doi/10.1021/acs.est.0c02906>.

Characterization, DFT calculations, O₂-TPD, photo-electrochemical measurements, EPR experiment, XRD patterns of samples (Figures S1 and S6), TEM and HRTEM images of BCN and BCN-C (Figures S2–S5 and S19), TG-MS signals of the gaseous components (Figure S7), XPS spectra of BCN and BCN-C (Figure S8), EPR spectra samples with different carbon contents (Figure S9), schematic illustration of the carbon-doping process (Figure S10), optical images (Figure S11), transient photocurrent response (Figure S12), valence-band XPS spectra (Figure S13), Mott-Schottky plots (Figure S14), chemical kinetic constant (Figure S15), N₂ adsorption-desorption isotherms and BET surface area data (Figure S18), toluene-TPD-MS profiles (Figure S20), oxygen-TPD profiles (Figure S21), EPR spectra of DMPO-•O₂⁻ (Figure S22), *in situ* DRIFTS spectra (Figures S23–S25), GC-MS profiles of toluene degradation (Figures S26 and S27) over BCN and BCN-C, gas toluene oxidation behavior of BCN-C and BCN with different carbon contents (Figure S16), degradation performance of BCN-C and C₃N₄ toward gas toluene (Figure S17), degradation performance of gas benzene (Figure S28) on BCN-C and BCN, atom percentage (Table S1), detailed bond information (Tables S2–S4) of BCN and BCN-C, recent works reported for photocatalytic degradation toward toluene (Table S5), and assigned species of corresponding bands for *in situ* DRIFTS spectra (Table S6) ([PDF](#))

■ AUTHOR INFORMATION

Corresponding Author

Dengsong Zhang — International Joint Laboratory of Catalytic Chemistry, Department of Chemistry, Research Center of Nano Science and Technology, College of Sciences, Shanghai University, Shanghai 200444, People's Republic of China; orcid.org/0000-0003-4280-0068; Phone: +86-21-66137152; Email: dszhang@shu.edu.cn

Authors

Wenqiang Qu — International Joint Laboratory of Catalytic Chemistry, Department of Chemistry, Research Center of Nano Science and Technology, College of Sciences, Shanghai University, Shanghai 200444, People's Republic of China

Penglu Wang — International Joint Laboratory of Catalytic Chemistry, Department of Chemistry, Research Center of Nano

Science and Technology, College of Sciences, Shanghai University, Shanghai 200444, People's Republic of China

Min Gao — Institute for Catalysis, Hokkaido University, Sapporo, Hokkaido 001-0021, Japan

Jun-ya Hasegawa — Institute for Catalysis, Hokkaido University, Sapporo, Hokkaido 001-0021, Japan; orcid.org/0000-0002-9700-3309

Zhi Shen — International Joint Laboratory of Catalytic Chemistry, Department of Chemistry, Research Center of Nano Science and Technology, College of Sciences, Shanghai University, Shanghai 200444, People's Republic of China

Qing Wang — International Joint Laboratory of Catalytic Chemistry, Department of Chemistry, Research Center of Nano Science and Technology, College of Sciences, Shanghai University, Shanghai 200444, People's Republic of China

Ruomei Li — International Joint Laboratory of Catalytic Chemistry, Department of Chemistry, Research Center of Nano Science and Technology, College of Sciences, Shanghai University, Shanghai 200444, People's Republic of China

Complete contact information is available at:

<https://pubs.acs.org/10.1021/acs.est.0c02906>

Author Contributions

[†]Wenqiang Qu and Penglu Wang contributed equally to this work.

Notes

The authors declare no competing financial interest.

■ ACKNOWLEDGMENTS

The authors acknowledge the support of the National Natural Science Foundation of China (21722704, 21976117, 21906102, and 21906101), the National Key R&D Program of China (2017YFE0132400), and the Shanghai Sailing Program (19YF1415300).

■ REFERENCES

- (1) Yang, G. H.; Wang, Y.; Zeng, Y. X.; Gao, G. F.; Liang, X. F.; Zhou, M. G.; Wan, X.; Yu, S. C.; Jiang, Y. H.; Naghavi, M.; Vos, T.; Wang, H. D.; Lopez, A. D.; Murray, C. J. L. Rapid health transition in China, 1990–2010: Findings from the Global Burden of Disease Study 2010. *Lancet* **2013**, *381* (9882), 1987–2015.
- (2) Li, H.; Shang, H.; Li, Y.; Cao, X.; Yang, Z.; Ai, Z.; Zhang, L. Interfacial Charging–Decharging Strategy for Efficient and Selective Aerobic NO Oxidation on Oxygen Vacancy. *Environ. Sci. Technol.* **2019**, *53* (12), 6964–6971.
- (3) Gao, Y.; Wang, H.; Zhang, X.; Jing, S. a.; Peng, Y.; Qiao, L.; Zhou, M.; Huang, D. D.; Wang, Q.; Li, X.; Li, L.; Feng, J.; Ma, Y.; Li, Y. Estimating Secondary Organic Aerosol Production from Toluene Photochemistry in a Megacity of China. *Environ. Sci. Technol.* **2019**, *53* (15), 8664–8671.
- (4) Wang, X.; Sun, M.; Muruganathan, M.; Zhang, Y.; Zhang, L. Electrochemically self-doped WO₃/TiO₂ nanotubes for photocatalytic degradation of volatile organic compounds. *Appl. Catal., B* **2020**, *260*, 118205.
- (5) Wang, F.; Deng, J.; Impeng, S.; Shen, Y.; Yan, T.; Chen, G.; Shi, L.; Zhang, D. Unraveling the effects of the coordination number of Mn over α-MnO₂ catalysts for toluene oxidation. *Chem. Eng. J.* **2020**, *396*, 125192.
- (6) Chen, Y.; Deng, J.; Yang, B.; Yan, T.; Zhang, J.; Shi, L.; Zhang, D. Promoting the Toluene Oxidation by Engineering the Octahedra Units via Oriented Insertion of Cu Ions in Tetrahedral Sites of MnCo Spinel Oxide Catalysts. *Chem. Commun.* **2020**, *56*, 6539.
- (7) Du, J.; Qu, Z.; Dong, C.; Song, L.; Qin, Y.; Huang, N. Low-temperature abatement of toluene over Mn-Ce oxides catalysts

- synthesized by a modified hydrothermal approach. *Appl. Surf. Sci.* **2018**, *433*, 1025–1035.
- (8) Qu, J.; Chen, D.; Li, N.; Xu, Q.; Li, H.; He, J.; Lu, J. Ternary photocatalyst of atomic-scale Pt coupled with MoS₂ co-loaded on TiO₂ surface for highly efficient degradation of gaseous toluene. *Appl. Catal., B* **2019**, *256*, 117877.
- (9) Weon, S.; He, F.; Choi, W. Status and challenges in photocatalytic nanotechnology for cleaning air polluted with volatile organic compounds: Visible light utilization and catalyst deactivation. *Environ. Sci.: Nano* **2019**, *6* (11), 3185–3214.
- (10) Kim, H. I.; Kim, H. N.; Weon, S.; Moon, G. H.; Kim, J. H.; Choi, W. Robust Co-catalytic Performance of Nanodiamonds Loaded on WO₃ for the Decomposition of Volatile Organic Compounds under Visible Light. *ACS Catal.* **2016**, *6* (12), 8350–8360.
- (11) Liu, J.; Li, Y.; Ke, J.; Wang, S.; Wang, L.; Xiao, H. Black NiO-TiO₂ nanorods for solar photocatalysis: Recognition of electronic structure and reaction mechanism. *Appl. Catal., B* **2018**, *224*, 705–714.
- (12) Li, J.; Dong, X. a.; Zhang, G.; Cui, W.; Cen, W.; Wu, Z.; Lee, S. C.; Dong, F. Probing ring-opening pathways for efficient photocatalytic toluene decomposition. *J. Mater. Chem. A* **2019**, *7* (7), 3366–3374.
- (13) Zhang, X.; Wang, L.; Zhou, X.; Ni, Z.; Xia, S. Investigation into the Enhancement of Property and the Difference of Mechanism on Visible Light Degradation of Gaseous Toluene Catalyzed by ZnAl Layered Double Hydroxides before and after Au Support. *ACS Sustainable Chem. Eng.* **2018**, *6* (10), 13395–13407.
- (14) Zou, X.; Yuan, C.; Dong, Y.; Ge, H.; Ke, J.; Cui, Y. Lanthanum orthovanadate/bismuth oxybromide heterojunction for enhanced photocatalytic air purification and mechanism exploration. *Chem. Eng. J.* **2020**, *379*, 122380.
- (15) Wang, H.; Wang, Y.; Jiang, C.; Ye, K.; He, X.; Xue, C.; Yang, Z.; Zhou, X.; Ji, H. Hybridization of CuO with Bi₂MoO₆ Nanosheets as a Surface Multifunctional Photocatalyst for Toluene Oxidation under Solar Irradiation. *ACS Appl. Mater. Interfaces* **2020**, *12* (2), 2259–2268.
- (16) Liu, J.; Wang, P.; Qu, W.; Li, H.; Shi, L.; Zhang, D. Nanodiamond-decorated ZnO catalysts with enhanced photocorrosion-resistance for photocatalytic degradation of gaseous toluene. *Appl. Catal., B* **2019**, *257*, 117880.
- (17) Ji, Y.; Zhao, J.; Terazono, H.; Misawa, K.; Levitt, N. P.; Li, Y.; Lin, Y.; Peng, J.; Wang, Y.; Duan, L.; Pan, B.; Zhang, F.; Feng, X.; An, T.; Marrero-Ortiz, W.; Secretst, J.; Zhang, A. L.; Shibuya, K.; Molina, M. J.; Zhang, R. Reassessing the atmospheric oxidation mechanism of toluene. *Proc. Natl. Acad. Sci. U. S. A.* **2017**, *114* (31), 8169–8174.
- (18) Zhang, W.; Li, G.; Liu, H.; Chen, J.; Ma, S.; Wen, M.; Kong, J.; An, T. Photocatalytic degradation mechanism of gaseous styrene over Au/TiO₂@CNTs: Relevance of superficial state with deactivation mechanism. *Appl. Catal., B* **2020**, *272*, 118969.
- (19) Tian, M. J.; Liao, F.; Ke, Q. F.; Guo, Y. J.; Guo, Y. P. Synergetic effect of titanium dioxide ultralong nanofibers and activated carbon fibers on adsorption and photodegradation of toluene. *Chem. Eng. J.* **2017**, *328*, 962–976.
- (20) Li, P.; Kim, S.; Jin, J.; Do, H. C.; Park, J. H. Efficient photodegradation of volatile organic compounds by iron-based metal-organic frameworks with high adsorption capacity. *Appl. Catal., B* **2020**, *263*, 118284.
- (21) Li, J. J.; Cai, S. C.; Xu, Z.; Chen, X.; Chen, J.; Jia, H. P.; Chen, J. Solvothermal syntheses of Bi and Zn co-doped TiO₂ with enhanced electron-hole separation and efficient photodegradation of gaseous toluene under visible-light. *J. Hazard. Mater.* **2017**, *325*, 261–270.
- (22) Wang, Y.; Yang, C.; Chen, A.; Pu, W.; Gong, J. Influence of yolk-shell Au@TiO₂ structure induced photocatalytic activity towards gaseous pollutant degradation under visible light. *Appl. Catal., B* **2019**, *251*, 57–65.
- (23) Lyu, J.; Zhou, L.; Shao, J.; Zhou, Z.; Gao, J.; Dong, Y.; Wang, Z.; Li, J. TiO₂ hollow heterophase junction with enhanced pollutant adsorption, light harvesting, and charge separation for photocatalytic degradation of volatile organic compounds. *Chem. Eng. J.* **2020**, *391*, 123602.
- (24) Zhang, Y.; Wu, M.; Kwok, Y. H.; Wang, Y.; Zhao, W.; Zhao, X.; Huang, H.; Leung, D. Y. C. In-situ synthesis of heterojunction TiO₂/MnO₂ nanostructure with excellent performance in vacuum ultraviolet photocatalytic oxidation of toluene. *Appl. Catal., B* **2019**, *259*, 118034.
- (25) Xie, R.; Lei, D.; Zhan, Y.; Liu, B.; Tsang, C. H. A.; Zeng, Y.; Li, K.; Leung, D. Y. C.; Huang, H. Efficient photocatalytic oxidation of gaseous toluene over F-doped TiO₂ in a wet scrubbing process. *Chem. Eng. J.* **2020**, *386*, 121025.
- (26) Weon, S.; Choi, W. TiO₂ Nanotubes with Open Channels as Deactivation-Resistant Photocatalyst for the Degradation of Volatile Organic Compounds. *Environ. Sci. Technol.* **2016**, *50* (5), 2556–2563.
- (27) Weon, S.; Choi, J.; Park, T.; Choi, W. Freestanding doubly open-ended TiO₂ nanotubes for efficient photocatalytic degradation of volatile organic compounds. *Appl. Catal., B* **2017**, *205*, 386–392.
- (28) Wang, H.; Dong, X. a.; Cui, W.; Li, J.; Sun, Y.; Zhou, Y.; Huang, H.; Zhang, Y.; Dong, F. High-surface energy enables efficient and stable photocatalytic toluene degradation via the suppression of intermediate byproducts. *Catal. Sci. Technol.* **2019**, *9* (11), 2952–2959.
- (29) Weon, S.; Choi, E.; Kim, H.; Kim, J. Y.; Park, H. J.; Kim, S. M.; Kim, W.; Choi, W. Active {001} Facet Exposed TiO₂ Nanotubes Photocatalyst Filter for Volatile Organic Compounds Removal: From Material Development to Commercial Indoor Air Cleaner Application. *Environ. Sci. Technol.* **2018**, *52* (16), 9330–9340.
- (30) Qin, J.; Wang, J.; Yang, J.; Hu, Y.; Fu, M.; Ye, D. Metal organic framework derivative-TiO₂ composite as efficient and durable photocatalyst for the degradation of toluene. *Appl. Catal., B* **2020**, *267*, 118667.
- (31) Bu, K.; Deng, J.; Zhang, X.; Kuboon, S.; Yan, T.; Li, H.; Shi, L.; Zhang, D. Promotional effects of B-terminated defective edges of Ni/boron nitride catalysts for coking- and sintering-resistant dry reforming of methane. *Appl. Catal., B* **2020**, *267*, 118692.
- (32) Bu, K.; Kuboon, S.; Deng, J.; Li, H.; Yan, T.; Chen, G.; Shi, L.; Zhang, D. Methane dry reforming over boron nitride interface-confined and LDHs-derived Ni catalysts. *Appl. Catal., B* **2019**, *252*, 86–97.
- (33) Cao, Y.; Maitarad, P.; Gao, M.; Taketsugu, T.; Li, H.; Yan, T.; Shi, L.; Zhang, D. Defect-induced efficient dry reforming of methane over two-dimensional Ni/h-boron nitride nanosheet catalysts. *Appl. Catal., B* **2018**, *238*, 51–60.
- (34) Luo, Z.; Fang, Y.; Zhou, M.; Wang, X. A Borocarbonitride Ceramic Aerogel for Photoredox Catalysis. *Angew. Chem., Int. Ed.* **2019**, *58* (18), 6033–6037.
- (35) Chen, L.; Zhou, M.; Luo, Z.; Wakeel, M.; Asiri, A. M.; Wang, X. Template-free synthesis of carbon-doped boron nitride nanosheets for enhanced photocatalytic hydrogen evolution. *Appl. Catal., B* **2019**, *241*, 246–255.
- (36) Zheng, M.; Yuan, T.; Shi, J.; Cai, W.; Wang, X. Photocatalytic Oxygenation and Deoxygenation Transformations over BCN Nanosheets. *ACS Catal.* **2019**, *9* (9), 8068–8072.
- (37) Manna, A. K.; Pati, S. K. Tunable Electronic and Magnetic Properties in B_xN_yC_z Nanohybrids: Effect of Domain Segregation. *J. Phys. Chem. C* **2011**, *115* (21), 10842–10850.
- (38) Gao, M.; Adachi, M.; Lyalin, A.; Taketsugu, T. Long Range Functionalization of h-BN Monolayer by Carbon Doping. *J. Phys. Chem. C* **2016**, *120* (29), 15993–16001.
- (39) Li, X.; Lin, B.; Li, H.; Yu, Q.; Ge, Y.; Jin, X.; Liu, X.; Zhou, Y.; Xiao, J. Carbon doped hexagonal BN as a highly efficient metal-free base catalyst for Knoevenagel condensation reaction. *Appl. Catal., B* **2018**, *239*, 254–259.
- (40) Huang, C.; Chen, C.; Zhang, M.; Lin, L.; Ye, X.; Lin, S.; Antonietti, M.; Wang, X. Carbon-doped BN nanosheets for metal-free photoredox catalysis. *Nat. Commun.* **2015**, *6* (1), 7698.
- (41) Yu, J.; Qin, L.; Hao, Y.; Kuang, S.; Bai, X.; Chong, Y. M.; Zhang, W.; Wang, E. Vertically Aligned Boron Nitride Nanosheets: Chemical Vapor Synthesis, Ultraviolet Light Emission, and Superhydrophobicity. *ACS Nano* **2010**, *4* (1), 414–422.

- (42) Ci, L.; Song, L.; Jin, C.; Jariwala, D.; Wu, D.; Li, Y.; Srivastava, A.; Wang, Z. F.; Storr, K.; Balicas, L.; Liu, F.; Ajayan, P. M. Atomic layers of hybridized boron nitride and graphene domains. *Nat. Mater.* **2010**, *9* (5), 430–435.
- (43) Aupic, C.; Abdou Mohamed, A.; Figliola, C.; Nava, P.; Tuccio, B.; Chouraqui, G.; Parrain, J.-L.; Chuzel, O. Highly diastereoselective preparation of chiral NHC-boranes stereogenic at the boron atom. *Chem. Sci.* **2019**, *10* (26), 6524–6530.
- (44) Toledo, J. R.; de Jesus, D. B.; Kianinia, M.; Leal, A. S.; Fantini, C.; Cury, L. A.; Sáfar, G. A. M.; Aharonovich, I.; Krambrock, K. Electron paramagnetic resonance signature of point defects in neutron-irradiated hexagonal boron nitride. *Phys. Rev. B: Condens. Matter Mater. Phys.* **2018**, *98* (15), 155203.
- (45) Gao, G.; Mathkar, A.; Martins, E. P.; Galvão, D. S.; Gao, D.; Autreto, P. A. d. S.; Sun, C.; Cai, L.; Ajayan, P. M. Designing nanoscaled hybrids from atomic layered boron nitride with silver nanoparticle deposition. *J. Mater. Chem. A* **2014**, *2* (9), 3148–3154.
- (46) Meng, S.; Ye, X.; Ning, X.; Xie, M.; Fu, X.; Chen, S. Selective oxidation of aromatic alcohols to aromatic aldehydes by BN/metal sulfide with enhanced photocatalytic activity. *Appl. Catal., B* **2016**, *182*, 356–368.
- (47) Wang, W.; Zhang, H.; Zhang, S.; Liu, Y.; Wang, G.; Sun, C.; Zhao, H. Potassium-Ion-Assisted Regeneration of Active Cyano Groups in Carbon Nitride Nanoribbons: Visible-Light-Driven Photocatalytic Nitrogen Reduction. *Angew. Chem., Int. Ed.* **2019**, *58* (46), 16644–16650.
- (48) Sun, X.; Luo, X.; Zhang, X.; Xie, J.; Jin, S.; Wang, H.; Zheng, X.; Wu, X.; Xie, Y. Enhanced Superoxide Generation on Defective Surfaces for Selective Photooxidation. *J. Am. Chem. Soc.* **2019**, *141* (9), 3797–3801.
- (49) Chen, X.; Chen, X.; Cai, S.; Chen, J.; Xu, W.; Jia, H.; Chen, J. Catalytic combustion of toluene over mesoporous Cr₂O₃-supported platinum catalysts prepared by in situ pyrolysis of MOFs. *Chem. Eng. J.* **2018**, *334*, 768–779.
- (50) Zhao, S.; Hu, F.; Li, J. Hierarchical Core-Shell Al₂O₃@Pd-CoAlO Microspheres for Low-Temperature Toluene Combustion. *ACS Catal.* **2016**, *6* (6), 3433–3441.
- (51) Sanati, M.; Andersson, A. DRIFT study of the oxidation and the ammonoxidation of toluene over a TiO₂(B)-supported vanadia catalyst. *J. Mol. Catal. A* **1993**, *81* (1), 51–62.
- (52) Yang, X.; Yu, X.; Lin, M.; Ma, X.; Ge, M. Enhancement effect of acid treatment on Mn₂O₃ catalyst for toluene oxidation. *Catal. Today* **2019**, *327*, 254–261.